Available online at www.sciencedirect.com

jmr&t Journal of Materials Research and Technology

journal homepage: www.elsevier.com/locate/jmrt

Partially recrystallized triplex-phase medium Mn steel strengthened by B2 precipitates

Jin-Young Kim [a], *Jin-Seob Kim* [a], *Taejin Song* [b], *Jin-Kyung Kim* [a,*]

[a] *Department of Materials Science and Chemical Engineering, Hanyang University, Ansan 15588, Republic of Korea*
[b] *Steel Products Research Group, Technical Research Laboratories, POSCO, Gwangyang 57807, Republic of Korea*

ARTICLE INFO

Article history:
Received 15 August 2023
Accepted 28 September 2023
Available online 1 October 2023

Keywords:
Medium Mn steel
B2 precipitates
Recovery
TRIP
Mechanical properties

ABSTRACT

We report the annealing time-dependent microstructure–mechanical properties relationship of cold-rolled and annealed Fe–6Mn-0.05C–3Ni-1.5Al (wt.%) steel, containing Ni and Al to form NiAl B2 precipitates. The microstructures of the investigated materials after cold-rolling and intercritical annealing show a mixture of lath and equiaxed zones consisting of a triplex matrix phase (ferrite, austenite, and tempered martensite) with B2 precipitates. Recovery of the deformed martensite in the cold-rolled microstructure during annealing resulted in the formation of sub-boundaries and a continuous transition from partially-recrystallized tempered martensite to recrystallized ferrite. The investigated materials showed a decrease in strength and an increase in ductility and strain-hardening rate with increasing annealing time. A decrease in the fraction of tempered martensite, an increase in the fraction of recrystallized ferrite/austenite grains, and enhanced transformation-induced plasticity (TRIP) kinetics with increasing annealing time led to enhanced ductility and strain hardening of the materials. The mixed presence of less stable equiaxed austenite and more stable lath austenite resulted in sustained TRIP effect during tensile deformation and superior strain hardening capacity of the specimen annealed for 24 h. This study provides a novel microstructure design solution for medium Mn steels, and further optimization of the composition and processing will lead to the development of medium Mn steels with superior mechanical performance.

1. Introduction

Lightweighting of automotive steel is essential to ensure fuel efficiency, environmental regulations, and passenger safety. Advanced high-strength steel (AHSS) can be lightweighted by using thinner sheets of ultrahigh-strength materials. However, the strength-ductility trade-off generally makes ultrahigh-strength materials less ductile. Medium Mn steels with 3–12 wt% Mn, a third-generation AHSS grade, have garnered significant research attention owing to their superior strength–ductility balance [1].

The microstructure of medium Mn steels typically consists of ultrafine ferrite and austenite after cold rolling and intercritical annealing [1]. Cold-rolled medium Mn steel generally exhibits a deformed martensitic microstructure, but upon intercritical annealing, the martensite partially reverses into austenite, and the retained martensite recrystallizes into ferrite [2]. The mechanical properties of medium Mn steels are largely dependent by the stability of austenite, which can be

* Corresponding author.
E-mail address: jinkyungkim@hanyang.ac.kr (J.-K. Kim).
https://doi.org/10.1016/j.jmrt.2023.09.299

controlled by varying the Mn and C concentrations in the steel [3]. Tunable stability of the retained austenite controls the activation of the transformation-induced plasticity (TRIP) or twinning-induced plasticity (TWIP) effects, leading to a superior strength–ductility balance [4,5]. Determining the optimal intercritical annealing conditions is essential for controlling the volume fraction and stability of austenite. The optimal intercritical annealing temperature of medium Mn steels has been reported to be slightly lower than the temperature yielding the maximum volume fraction of retained austenite at room temperature, leading to the absence of athermal martensite and a gradual TRIP effect upon tensile deformation [2].

The yield strength (YS) of medium Mn steels can be improved through precipitation strengthening [6–8]. Recently, B2-phase-strengthened medium Mn steels [9–14] have been reported among the various forms of precipitates. The addition of Ni and Al to these steels led to the formation of nanoscale B2 intermetallic precipitates and enhanced YS of the materials. While several previous studies [11–14] have reported the formation of B2 precipitates in δ-ferrite formed by Al alloying in medium Mn steels, the precipitates were also formed in ferrite and austenite of medium Mn steels [10,14]. The cold-rolled and intercritically annealed Fe-7.2Mn-0.22C-3.1Al-2.9Ni (wt.%) steel showed precipitation of 2–140 nm B2 particles at the phase boundaries and interiors of ferrite and austenite, and the material exhibited a superior combination of mechanical properties, i.e., a YS of 855 MPa, ultimate tensile strength (UTS) of 961 MPa, and total elongation (TE) of 53% by combined effect of precipitation strengthening and TRIP effect [10].

We designed a low-carbon medium Mn steel favorable for weldability and reduced plastic instability characterized by the Portevin–LeChatelier (PLC) effect. Medium Mn steels often show partially recrystallized microstructures after cold rolling and intercritical annealing, which could enhance the YS of the materials [15,16]. The present study combines partially recrystallized microstructures and B2 precipitation strengthening to obtain superior mechanical properties of the investigated material after cold rolling and intercritical annealing. We focused on elucidating the relationship between the annealing time-dependent microstructures and the mechanical properties of the cold-rolled and annealed materials.

2. Experimental

The chemical composition of the investigated material was measured using inductively coupled plasma (ICP) analysis as Fe-5.60Mn-0.047C-3.12Ni-1.49Al (wt.%). The ingot was produced by vacuum induction melting. Slabs produced from the ingots were solution-treated at 1200 °C for 2 h and hot-rolled to a thickness of 3 mm. The hot-rolled specimens were further cold-rolled to a thickness of 1.5 mm. The cold-rolled materials were annealed at 620 °C for 1, 2, 5, 10, and 24 h, followed by water quenching. Herein, the cold-rolled materials annealed at 620 °C for 1, 2, 5, 10, and 24 h are referred to as IA620-1, IA620-2, IA620-5, IA620-10, and IA620-24, respectively.

The phase analysis of the investigated materials was conducted using X-ray diffraction (XRD; D-MaX/2500-PC, Rigaku) in the 2θ range of 30–100° with a Cu source at a scanning speed of 4°/min. The microstructures were characterized using scanning electron microscopy (SEM; MIRA3, TESCAN), electron backscatter diffraction (EBSD), and transmission electron microscopy (TEM). The samples for XRD, SEM, and EBSD analyses were electropolished (20 V, 15 °C) in a mixture of 90% acetic acid and 10% perchloric acid. The local chemical composition of the material was investigated using SEM with energy-dispersive X-ray spectroscopy (EDS). The EBSD patterns were recorded using an EDAX TSL detector attached to a TESCAN Mira 3 SEM operated at 15–18 kV. The step size of the EBSD scans was 25 nm. The OIM analysis software was used to analyze EBSD data. TEM characterization was performed using a JEOL JEM-2100F instrument equipped with an EDS detector and operated at 200 kV. The TEM specimens were prepared using a focused ion beam (FIB) in a field-emission SEM (FEI Scios) and also prepared as 3 mm diameter disks, which were mechanically polished to a thickness of less than 80 μm and thinned by an electrolytic double-jet technique at −30 °C. A mixture of 5% perchloric acid and 95% ethanol was used as the electrolyte. Bright-field (BF) images, high-resolution TEM (HR-TEM) images, and diffraction patterns (DPs) were acquired for the TEM characterization. Tensile tests were conducted at room temperature using a universal testing machine (MINOS-100, MTDI) at a strain rate of 10^{-3} s^{-1}. ASTM E8 sub-size tensile specimens with gauge dimensions of 25 × 6 × 1.5 mm were prepared with the long axis aligned with the rolling direction.

3. Results

3.1. *Intercritical annealing temperature-dependent volume fraction of austenite*

The volume fraction of austenite changes depending on the annealing temperature. Fig. 1 shows the intercritical annealing temperature-dependent austenite volume fraction for the annealing time of 1 h. The austenite volume fraction increases with increasing annealing temperature up to 640 °C and then decreases when the intercritical annealing temperature exceeds 640 °C. The annealing temperature producing the maximum austenite fraction is 640 °C, with an austenite volume fraction of 28%. The decrease in austenite volume fraction for annealing temperatures higher than 640 °C resulted from the transformation from austenite to martensite upon cooling. The sample annealed at 700 °C contains an austenite volume fraction of less than 5%, indicating that most austenite grains were transformed to martensite. The optimal intercritical annealing temperature leading to the highest strength–ductility balance of medium Mn steels has been reported to be slightly lower than the temperature with the maximum austenite fraction [2]. Thus, we selected an annealing temperature of 620 °C, which is slightly lower than the annealing temperature with the maximum austenite fraction (640 °C).

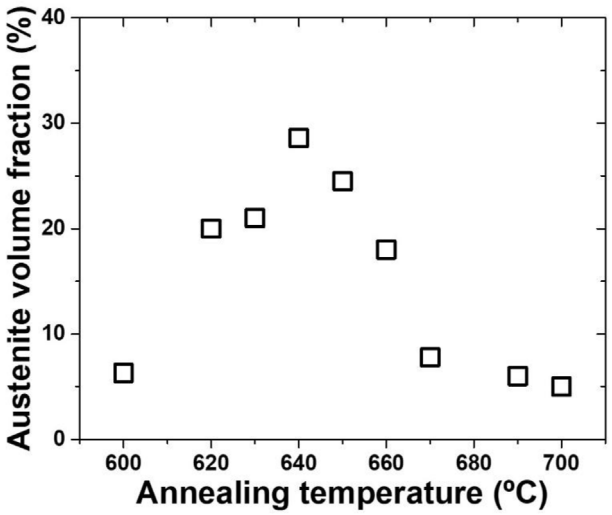

Fig. 1 – Variation in the austenite volume fraction after intercritical annealing at various temperatures for 1 h. The annealing temperature of 640 °C yields the maximum austenite volume fraction of 28%.

3.2. *Annealing time-dependent microstructures*

The SEM micrographs of specimens after intercritical annealing at 620 °C for various durations are shown in Fig. 2. In the SEM micrographs, the red, green, and sky-blue arrows represent martensite, austenite, and ferrite, respectively. The cold-rolled steel contains deformed martensite and a small amount of lath-shaped retained austenite (Fig. 2(a)). Whereas the cold-rolled material mainly shows a lath-shaped microstructure (Fig. 2(a_2)), the annealed materials exhibit a mixture of lath zone consisting of tempered martensite and lath austenite (Fig. 2(b_2)–(d_2)) and equiaxed zones consisting of equiaxed ferrite, equiaxed austenite, and tempered martensite (Fig. 2(b_3)–(d_3)). With increasing annealing time, the lath zone and the equiaxed zone tend to decrease and increase, respectively. The lath austenite could be reverse-transformed from the deformed martensite during the recovery process (Fig. 2(b_2)–(d_2)) [17]. Recrystallization of deformed martensite could lead to the nucleation of fine equiaxed ferrite and austenite [18]; thus, the equiaxed zone increases with increasing annealing time (Fig. 2(b_3)–(d_3)). All the SEM micrographs show nanoscale precipitates as a white contrast, and these are mostly present in the tempered martensitic phase.

The elemental concentration distribution was investigated by the SEM-EDS analysis of the lath and equiaxed zones of specimens IA620-10 and IA620-24 (Fig. 3). The EDS line scan was conducted along the yellow lines, and the plots of Mn, Ni, and Al concentrations depending on the location are overlaid on the SEM micrographs. For all the investigated conditions, austenite exhibits higher Mn and Ni contents and a lower Al content than the surrounding ferrite/tempered martensite.

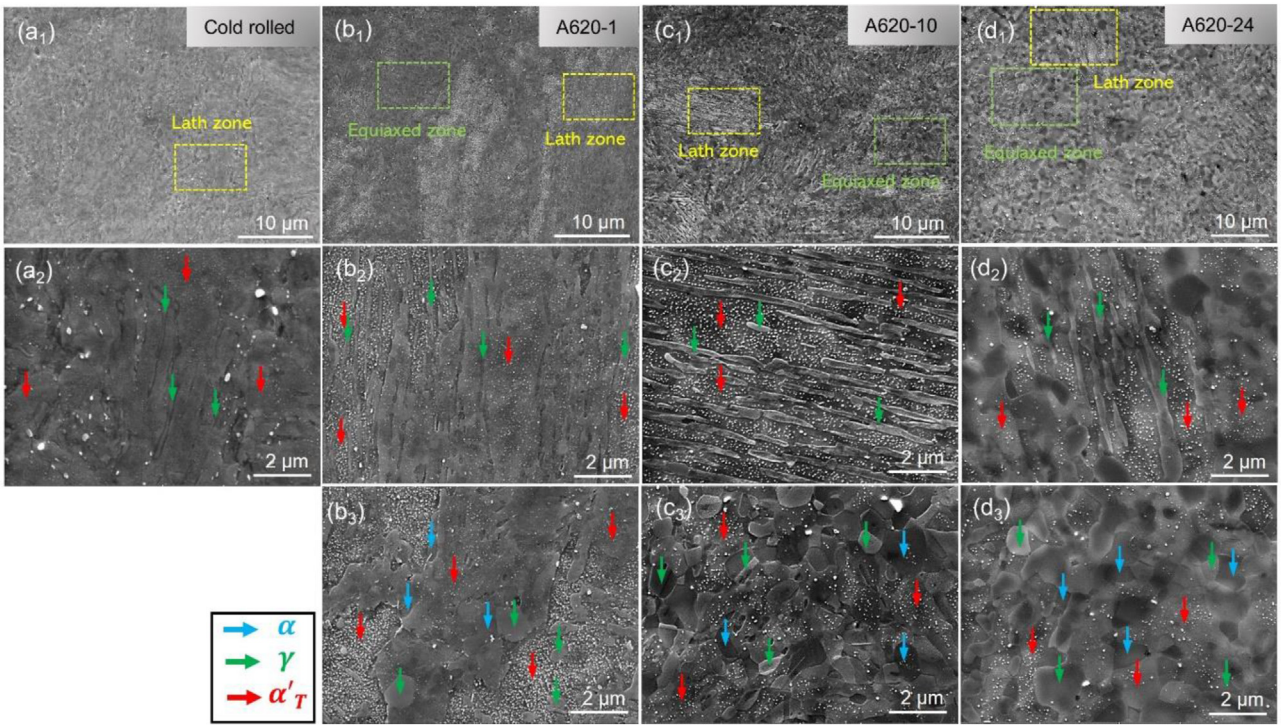

Fig. 2 – SEM microstructural evolution of (a) the cold-rolled material, (b) IA620-1, (c) IA620-10, and (d) IA620-24. The microstructure shows a mixture of lath and equiaxed zones. The red, green, and sky-blue arrows represent martensite, austenite, and ferrite, respectively. The annealed materials show a mixture of lath (a_2)–(d_2) and equiaxed (b_3)–(d_3) zones. All the SEM micrographs show the nanoscale precipitates as a white contrast, and these are mostly present in the martensitic matrix.

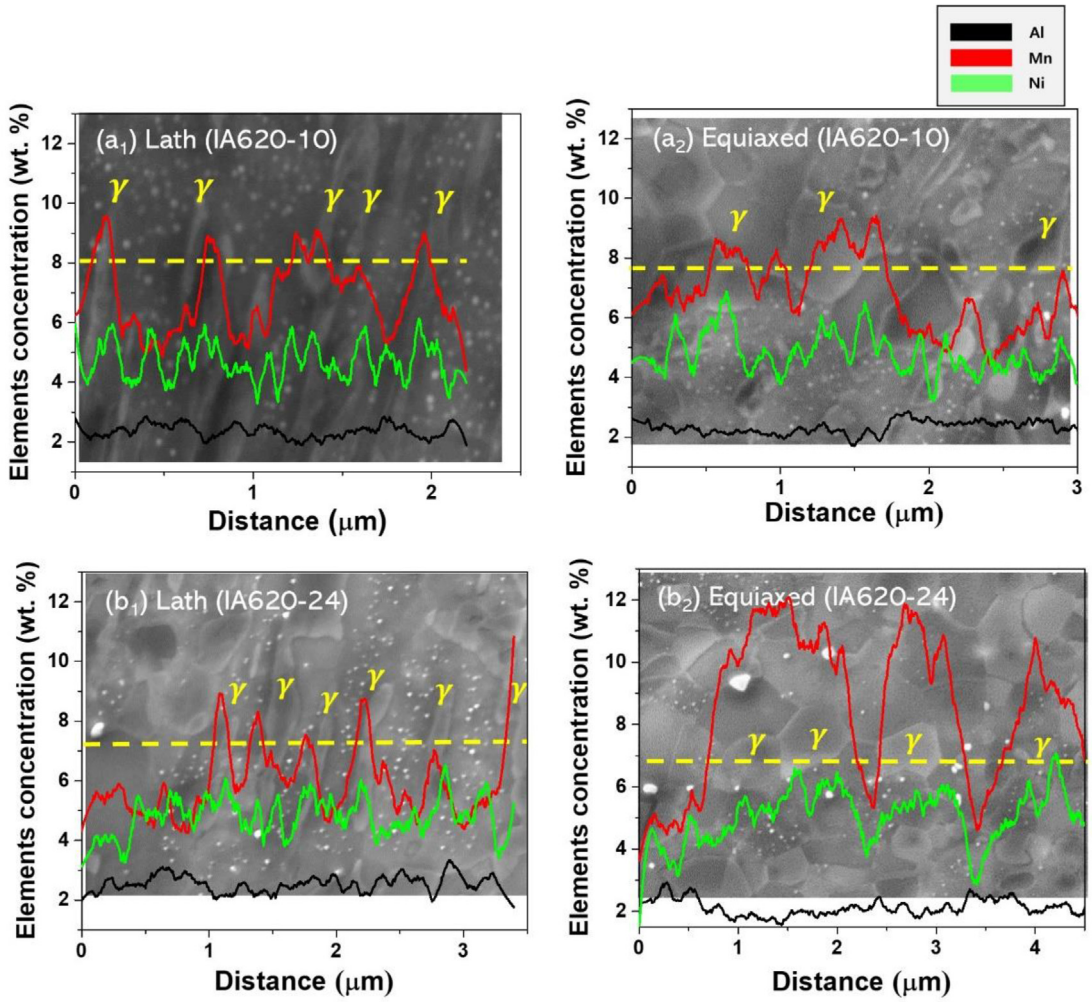

Fig. 3 – Elemental concentration distributions obtained using SEM-EDS analysis for the lath and equiaxed zones of specimens IA620-10 and IA620-24. The EDS line scan is conducted along the yellow line, and the plots of the Mn, Ni, and Al concentrations depending on the location are overlaid on the SEM micrographs. Austenite shows higher Mn and Ni contents and a lower Al content than the surrounding ferrite/tempered martensite. The Mn concentration range is 8–12 wt%, Ni concentration range is 4–6 wt%, and Al concentration is less than 1.5 wt%.

The Mn concentration range is 8–12 wt%, the Ni concentration range is 4–6 wt.%, and the Al concentration is less than 1.5 wt%.

More quantitative concentration distributions of Mn, Ni, and Al in the recrystallized equiaxed ferrite and austenite of specimens IA620-10 and IA620-24 are listed in Table 1. More than 40 points for each condition were investigated through point analysis of the SEM-EDS. Austenite exhibits higher Mn and Ni contents and a lower Al content than ferrite. Specimen IA620-24 shows a slightly lower Mn content than that of specimen IA620-10, probably because of the higher austenite volume fraction of the former specimen.

Fig. 4 shows the EBSD analysis of the annealed materials. The EBSD phase maps (Fig. 4(a_1)–(e_1)) show the distribution of the austenite grains, indicating their increase in both size and fraction. The grain orientation spread (GOS) maps of the body-centered cubic (BCC) phase (Fig. 4(a_2)–(e_2)) were used to distinguish the recrystallized grains from the partially recrystallized grains. Deformation of the material leads to distortion of the grains and a high GOS value, whereas recrystallized grains exhibit a low GOS value of close to zero [19]. The reported threshold GOS values distinguishing recrystallized and deformed grains range from 1 to 2° [20,21]. In the present study, grains with a GOS value of less than 2° (blue) and those with a GOS value of greater than 2° (red) are considered recrystallized and partially recrystallized grains, respectively. The presence

Table 1 – Quantitative concentration distributions of Mn, Ni, and Al in the recrystallized equiaxed ferrite and austenite of specimens IA620-10 and IA620-24, as measured by SEM-EDS analysis.

Concentration (wt.%)	Phase	Mn	Ni	Al
IA620-10	α	5.87 ± 2	3.22 ± 1	1.74 ± 2
	γ	9.70 ± 1	4.51 ± 4	1.45 ± 2
IA620-24	α	4.76 ±3	2.77 ± 3	1.85 ± 3
	γ	9.30 ± 1	4.16 ± 2	1.43 ± 1

of prior austenite grains formed during homogenization and hot rolling is evidenced by the partially-recrystallized regions exhibiting the same orientation in the inverse pole figure (IPF) maps (Fig. 4(a_3)–(e_3)). Fig. 4(f) shows the annealing time-dependent average grain size and volume fraction of austenite, as determined by the EBSD analysis. With increasing annealing time, the grain size and volume fraction of austenite increase owing to an increased degree of recrystallization and grain growth. The distribution of boundary misorientation is shown in the BCC GOS map of the specimen IA620-24 (Fig. 4(g)). The green and yellow lines represent the low-angle boundaries with misorientation angles in the range of 2–15° and high-angle boundaries with misorientation angles higher than 15°, respectively. The recrystallized grains (blue) tend to be

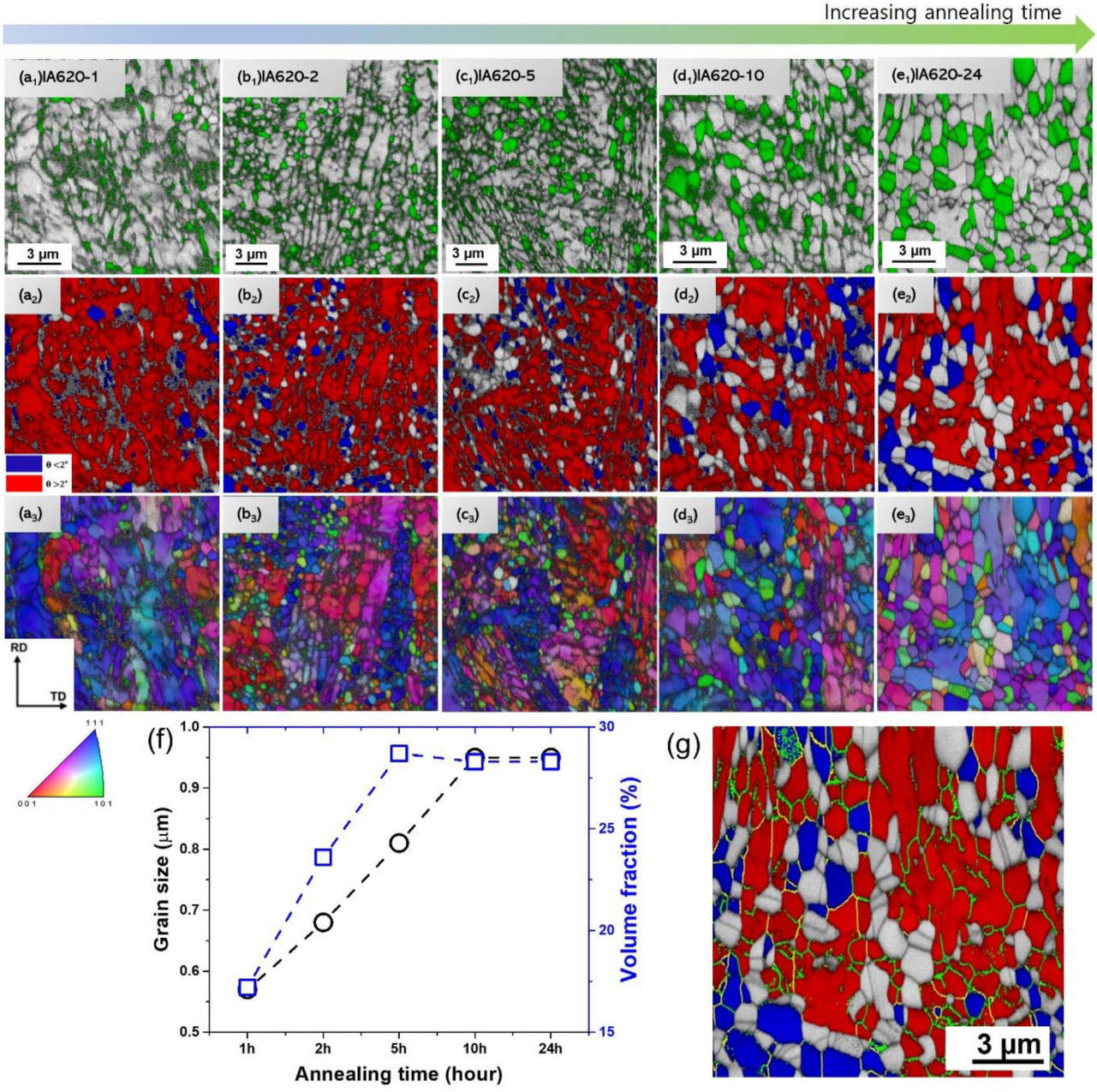

Fig. 4 – EBSD analysis of the annealed materials. (a_1)–(e_1) EBSD phase maps showing the distribution of the equiaxed austenite grains (green), indicating their increase in both size and fraction. (a_2)–(e_2) Gain orientation spread (GOS) maps of the BCC phase showing the recrystallized (blue, GOS <2°) and partially recrystallized grains (red, GOS >2°). (a_3)–(e_3) Inverse pole figure (IPF) maps showing the presence of prior austenite grains formed during homogenization and hot rolling, exhibiting the same orientation. (f) Annealing time-dependent average grain size and volume fraction of austenite, as determined by EBSD analysis. (g) BCC GOS map of the specimen IA620-24, showing the distribution of boundary misorientation. The green and yellow lines represent the low-angle boundaries with misorientation angles in the range of 2–15° and high-angle boundaries with misorientation angles higher than 15°, respectively.

surrounded by high-angle grain boundaries, whereas a high density of low-angle boundaries is present in the partially-recrystallized grains, indicating a continuous transition from partially-recrystallized tempered martensite to recrystallized ferrite.

The direct evidence of the recovery process is provided by TEM analysis of specimens IA620-10 and IA620-24 (Fig. 5). Fig. 5(a) shows a tempered martensite grain exhibiting the recovery process of specimen IA600-10. Regions (1) and (2) show a BCC structure with a slight misorientation of 4.0° with respect to the [001] zone axis, as determined from the overlaid DP obtained from regions (1) and (2) divided by the sub-boundary consisting of dislocations (yellow arrows). A similar feature is also observed for specimen IA600-24 (Fig. 5(b)). The grain shows dislocation structures and a sub-boundary consisting of a high density of dislocations (yellow arrows). Regions (1) and (2) show a BCC structure with a slight misorientation of 1.6° with respect to the [110] zone axis, as determined from the overlaid DP obtained from regions (1) and (2) divided by the sub-boundary. Interestingly, the right side of the sub-boundary shows parallel long dislocations on the {112} trace, indicating dislocations present on the {112} slip plane.

Detailed TEM characterization of the lath zone and equiaxed zone was conducted for specimen IA620-24 (Fig. 6). The overview image of the lath zone (Fig. 6(a_1)) shows a high defect density. The zoomed-in image obtained from the red box in Fig. 6(a_1) and the DPs obtained from the dashed circles 1–4 (Fig. 6(a_2)) show a mixed presence of the BCC tempered martensite and the face-centered cubic (FCC) lath austenite. The tempered martensite grains are characterized by the frequent presence of dislocations and precipitates. Fig. 6(b) shows the overview image of the equiaxed zone and the DPs obtained from the dashed circles 1–6, confirming a mixed presence of the BCC ferrite/tempered martensite and the FCC austenite. The defect density is low in the equiaxed zone. The representative precipitates are indicated by the yellow arrows.

3.2. B2 precipitation behavior

An overview of the distribution of the precipitates is shown in the SEM micrograph of specimen IA620-24 (Fig. 7(a_1)). The zoomed-in image (Fig. 7(a_2)) of the yellow dashed box in Fig. 7(a_1) shows a higher density of precipitates in the tempered martensite than in the recrystallized ferrite/austenite grains. The precipitates in the phase/grain boundaries (yellow arrows) are coarser than those in the grain interior. TEM analysis was conducted for specimen IA600-24 to characterize the observed precipitates in detail. Fig. 7(b) provides the BF TEM image of the 5% deformed specimen IA620–24, showing the presence of the B2 precipitates located at the interior of a BCC matrix. The DP obtained from the dashed circle in the image shows a similar BCC pattern of the [111] zone axis with a slightly different magnitude of diffraction vectors, owing to the similar crystal structure of the B2 precipitates and BCC matrix. The B2 phase shows smaller {110} spacing in the reciprocal lattice than the BCC matrix, indicating a larger lattice parameter of the former, which is consistent with a previous study [22]. Fig. 7(c) presents the HR-TEM image showing a B2 particle in the BCC matrix. The zoomed-in image obtained from the blue and yellow boxes and the corresponding fast Fourier transformation (FFT) patterns confirm the similar atomic arrangement of the BCC structure for both regions. The measured {110} interplanar spacing of the matrix and the particle is 0.236 nm and 0.244 nm, respectively, confirming the larger lattice parameter of the B2 phase than the BCC matrix. Scanning transmission

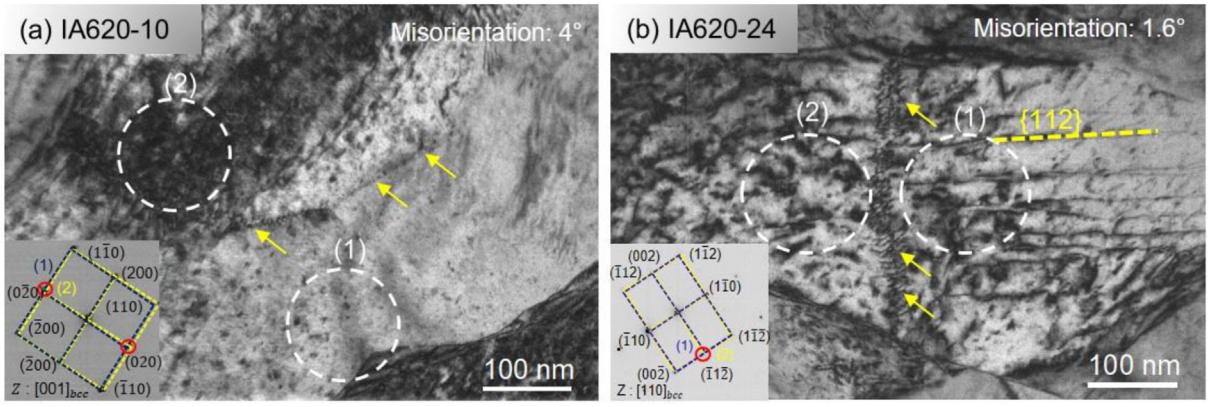

Fig. 5 – TEM analysis of specimens IA620-10 and IA620-24. (a) Tempered martensite grain exhibiting the recovery process of specimen IA620-10. Regions (1) and (2) show a BCC structure with a slight misorientation of 4.0° with respect to the [001] zone axis, as determined from the overlaid DP obtained from regions (1) and (2) across the sub-boundary indicated by the yellow arrows. The sub-boundary consists of a high density of dislocations, as indicated by the yellow arrows. (b) Tempered martensite grain exhibiting the recovery process of specimen IA620-24. The grain shows dislocation structures and a sub-boundary consisting of a high density of dislocations, as indicated by the yellow arrow. Regions (1) and (2) show a BCC structure with a slight misorientation of 1.6° with respect to the [110] zone axis, as determined from the overlaid DP obtained from regions (1) and (2) across the sub-boundary indicated by the yellow arrows. The right side of the sub-boundary shows parallel long dislocations present on the {112} trace, indicating dislocations on the {112} slip plane.

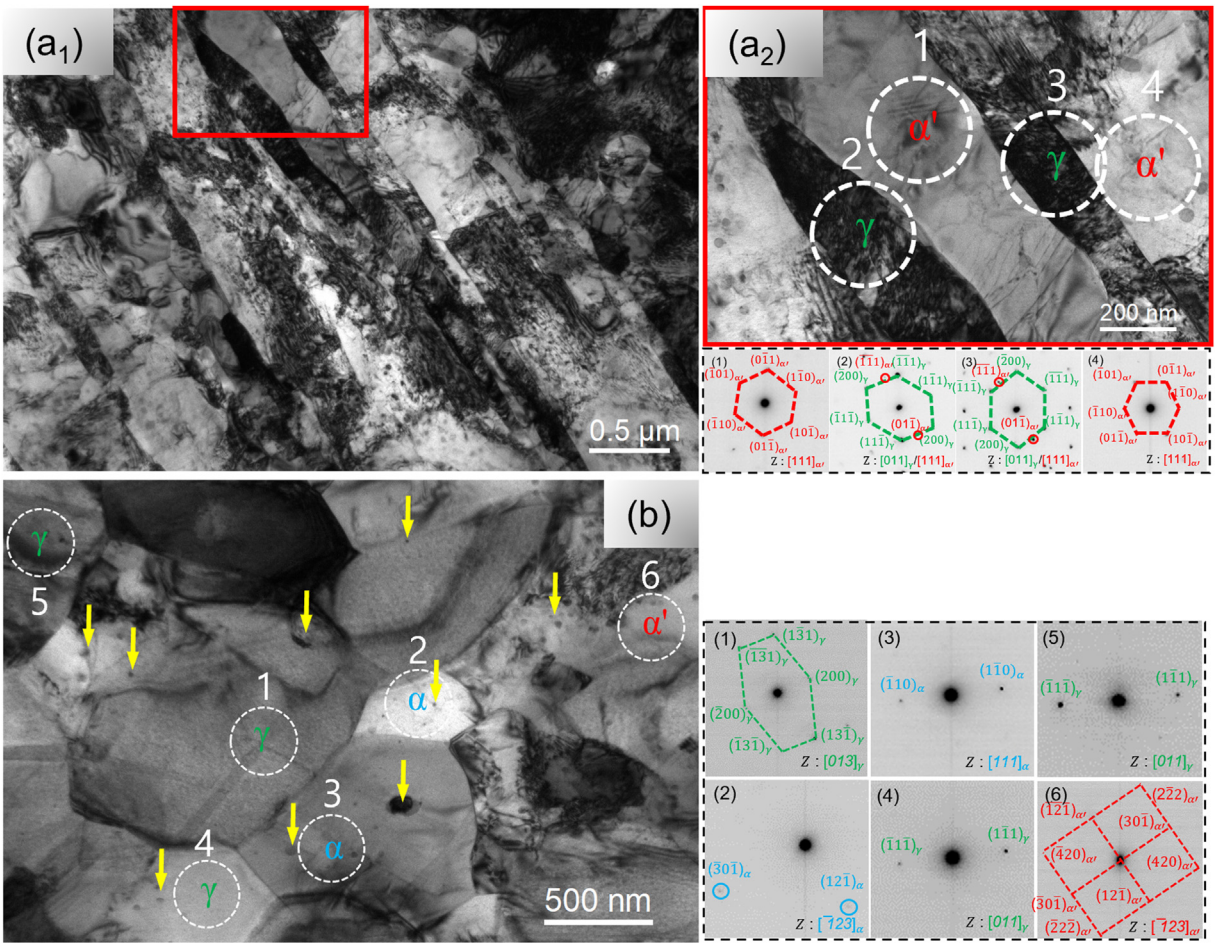

Fig. 6 – TEM analysis of specimens IA620-24. (a_1) Overview image of the lath zone showing a high defect density. (a_2) Zoomed-in image obtained from the red box in (a_1) and the DPs obtained from the dashed circles 1–4, showing a mixed presence of the BCC tempered martensite and the FCC lath austenite. (b) Overview image of the equiaxed zone and the DPs obtained from the dashed circles 1–6, confirming a mixed presence of the BCC ferrite/tempered martensite and the FCC austenite. The representative precipitates are indicated by the yellow arrows.

electron microscopy (STEM)-EDS analysis was performed to investigate the elemental distribution of specimen IA620-24 (Fig. 7(d)). The EDS elemental maps show the area consisting of the Mn-enriched and the Mn-depleted area. The Mn-enriched and the Mn-depleted areas are expected to be an austenite grain and a ferrite/martensite grain, respectively. In the ferrite/martensite grain, Ni-rich particles are observed (indicated by the yellow arrows).

3.4. *Annealing-time dependent mechanical properties and TRIP effect*

The annealing time-dependent mechanical properties of the annealed specimens are shown in Fig. 8. The engineering stress–strain curves of the investigated materials show a decrease in strength and an increase in ductility with increasing annealing time (Fig. 8(a)). Specimen IA620-10 shows a YS of 746 MPa, UTS of 904 MPa, and TE of 17.7%, whereas specimen IA620-24 shows a YS of 692 MPa, UTS of 848 MPa, and TE of 24.5%. Fig. 8(b) compares the strain-hardening rate curves of the investigated steels. The strain-hardening rate increases with increasing annealing time; thus, specimen IA620-24 exhibits a higher strain-hardening rate than specimen IA620-10. The tensile properties of the investigated materials are summarized in Table 2.

XRD and EBSD analyses were conducted to investigate the TRIP effect (Fig. 9). Fig. 9(a) shows the volume fraction of retained austenite before and after tensile deformation under different annealing conditions. The TRIP effect leads to a decrease in the austenite fraction after tensile deformation under all annealing conditions. The volume fraction of austenite transformed to martensite is estimated from the ratio between the austenite fraction transformed to martensite in the fractured condition and the initial austenite fraction in the as-annealed condition (Fig. 9(b)). The volume fraction of austenite transformed to martensite increases

with increasing annealing time. The fractured IA620-24 sample shows almost no retained austenite, indicating that most of the austenite grains present in the annealed microstructure were transformed to martensite. EBSD analysis was conducted for the annealed, 5% deformed, and 10% deformed IA620-10 and IA620-24 specimens. The EBSD phase maps of IA620-10 (Fig. 9(c_1)–(c_3)) and IA620-24 (Fig. 9(d_1)–(d_3)) confirm a continuous decrease in the austenite volume fraction with increasing strain owing to the TRIP effect.

3.5. *Deformation mechanisms*

TEM analysis was conducted for the 5% deformed IA620-24 specimen to investigate the various deformation mechanisms

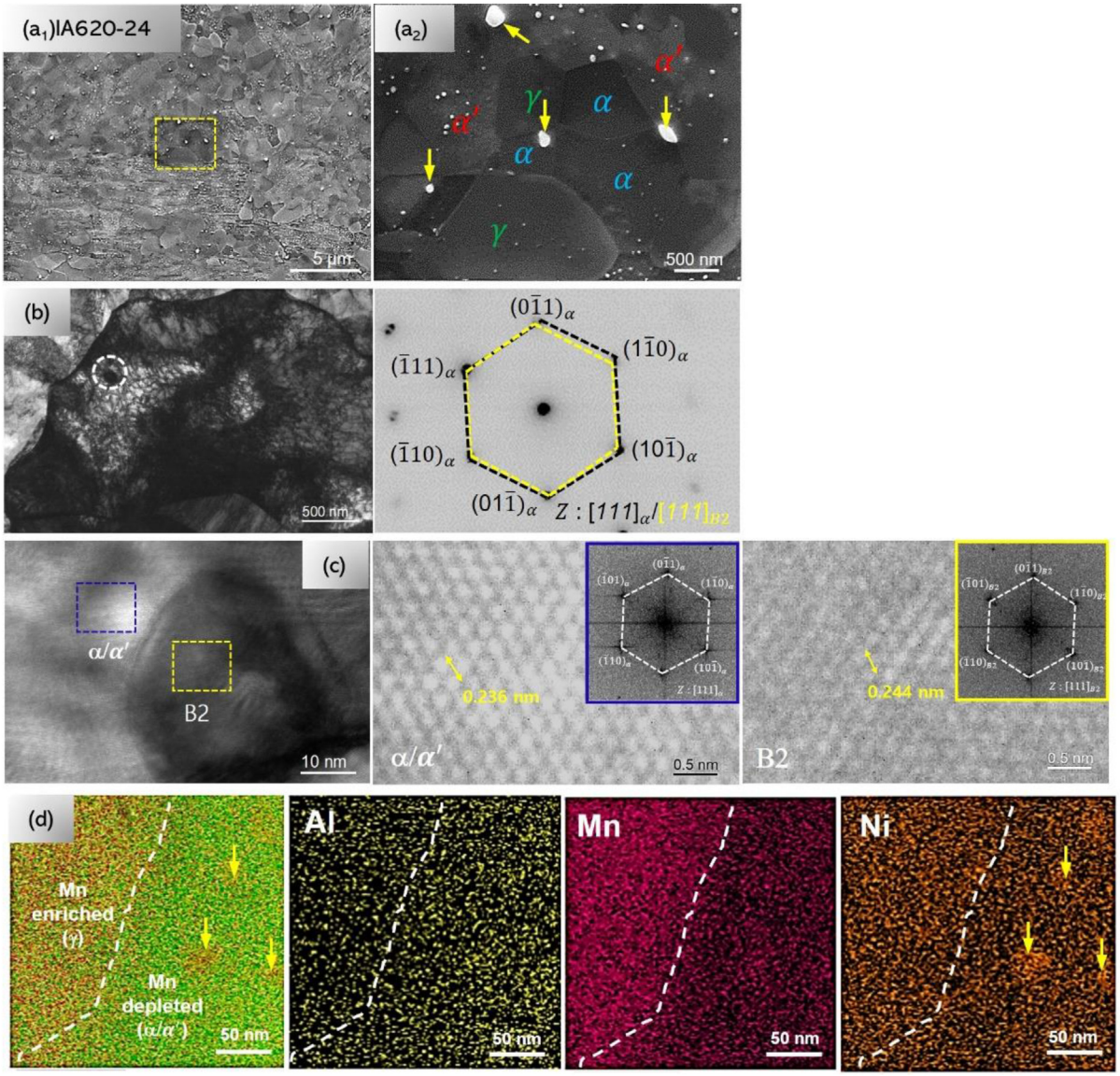

Fig. 7 – SEM/TEM characterization of the precipitates in specimen IA620-24. (a_1) SEM image showing an overview of the distribution of precipitates in the IA620-24 sample. (a_2) Zoomed-in image of the yellow dashed box in (a_1) showing a higher density of precipitates in the tempered martensite than in the recrystallized ferrite/austenite grains. The precipitates in the phase/grain boundaries (yellow arrows) are coarser than those in the grain interior. (b) BF TEM image and DP obtained from the 5% deformed specimen IA620–24, confirming the presence of the B2 precipitates located at the interior of a BCC matrix. The DP shows a similar BCC pattern of the [111] zone axis with a slightly different magnitude of diffraction vectors, owing to the similar crystal structure of the B2 precipitates and BCC matrix. (c) HR-TEM image showing a B2 particle in the BCC matrix. The zoomed-in image obtained from the blue (matrix) and yellow (particle) boxes and the corresponding fast Fourier transformation (FFT) patterns confirm the similar atomic arrangement of the BCC structure for both regions. (d) STEM-EDS elemental maps showing the area consisting of an austenite grain (the Mn enriched area) and a ferrite/martensite grain (the Mn depleted area). In the ferrite/martensite grain, Ni-rich particles are observed (indicated by the yellow arrows).

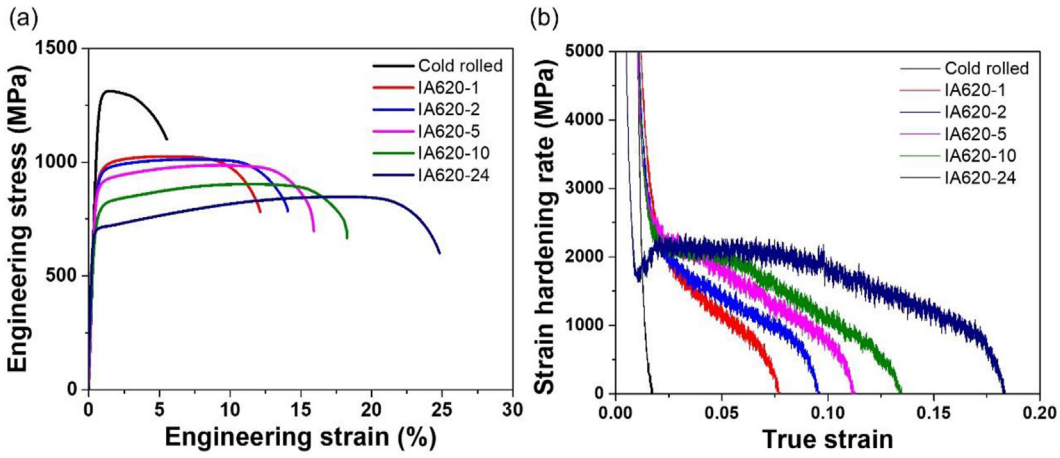

Fig. 8 – Annealing time-dependent mechanical properties of the investigated materials. (a) Engineering stress–strain curves, showing a decrease in strength and an increase in ductility with increasing annealing time. (b) Strain hardening rate curves of the investigated steels. The strain hardening rate increases with increasing annealing time.

operative in the equiaxed austenite grains (Fig. 10(a)-(c)). The grain in Fig. 10(a) shows a high density of thin plates present parallel to the $(11\bar{1})$ plane, and the streak in the corresponding DP suggests that the thin plates correspond to stacking faults. The grain in Fig. 10(b) also shows a high density of thin plates present parallel to the $(11\bar{1})$ plane, and the corresponding DP confirms that the plates correspond to the hexagonal close-packed (HCP) ε-martensite, which grows by the motion of Shockley partial dislocations on every second {111} plane [23]. At the intersection of the plate-type defects in the austenite grain in Fig. 10(c), the presence of α' martensite was confirmed.

Deformation mechanisms operative in the lath austenite grains of the 5% deformed IA620-24 specimen were also investigated by TEM (Fig. 10(d)–(e)). The lath austenite grain in Fig. 10(d) shows the high defect density and the corresponding DP shows the single FCC pattern without the occurrence of phase transformation. The lath austenite grain in Fig. 10(e) shows parallel plate-type defects and the corresponding DP confirms that they are deformation twins. Purple circles indicate diffraction spots corresponding to the deformation twin.

Deformation mechanisms of the tempered martensite /ferrite in the 5% deformed IA620-24 specimen were also investigated by TEM analysis (Fig. 11). Complex dislocation arrangement is present in the tempered martensite grain in Fig. 11(a), indicating that dislocation multiplication is the main deformation mechanism of the tempered martensite. The interactions between dislocations and B2 particles, which contribute to precipitation strengthening, are observed in the ferrite/martensite grain in Fig. 11(b).

3.6. *Damage and fracture characteristics*

The damage behavior of specimen IA620-24 was investigated based on SEM analysis of the fractured microstructure. Voids or cracks are observed in the lath zone (Fig. 12(a)) and equiaxed zone (Fig. 12(b)). Both regions show the tempered martensite grains decorated with a high density of white B2 particles. The voids or cracks indicated by the yellow arrows are associated with the austenite/martensite phase boundaries. Voids or cracks present near the B2 particles are indicated by red arrows; however, their size remains small compared to the voids or cracks near the phase boundaries. This indicates the superior damage resistance of the fine B2 precipitates.

Fractography analysis was conducted for all the investigated materials (Fig. 13). Fig. 13(a_1)–(f_1) provide an overview of the fracture surfaces of the investigated materials. All the investigated materials exhibit a mixture of ductile (Fig. 13(a_2)–(f_2)) and

Table 2 – Summary of the tensile properties of the investigated materials. (UE: uniform elongation).

Annealing time (h)	YS (MPa)	UTS (MPa)	UE (%)	TE (%)	UTS × TE (MPa;%)
C.R	1236 ± 7	1313 ± 3	1.8 ± 0.5	6.1 ± 1	8009
IA620-1	912 ± 8	1026 ± 5	5.0 ± 0.1	11.7 ± 0.5	12,004
IA620-2	895 ± 6	1013 ± 2	7.5 ± 0.5	13.9 ± 0.1	14,080
IA620-5	848 ± 6	986 ± 5	9.0 ± 0.4	15.6 ± 0.8	15,411
IA620-10	746 ± 7	904 ± 6	14 ± 3	17.7 ± 3	16,000
IA620-24	692 ± 7	848 ± 7	16.3 ± 1	24.5 ± 1	20,776

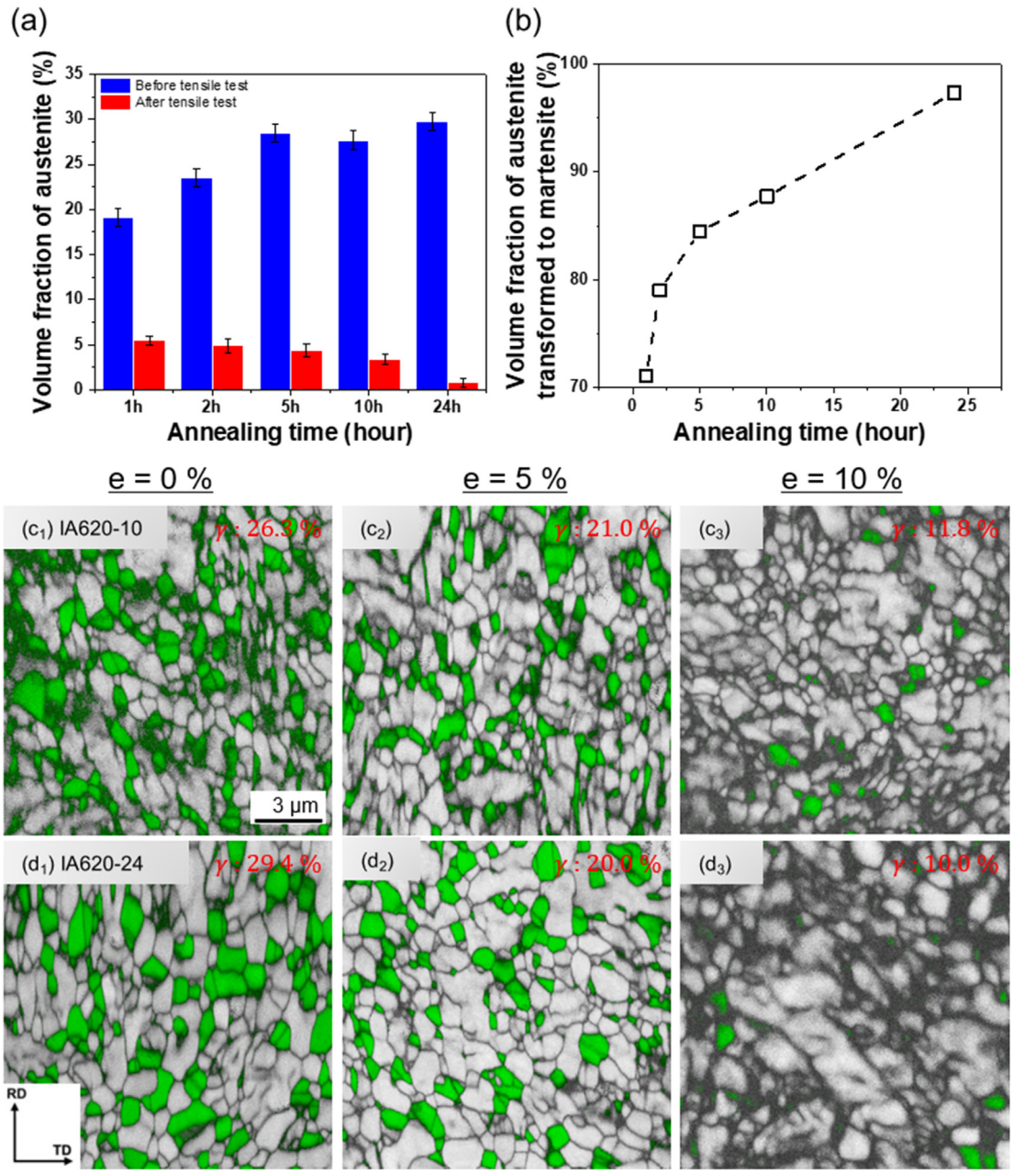

Fig. 9 – (a) Volume fractions of retained austenite before and after tensile deformation for different annealing conditions. The TRIP effect leads to a decrease in the austenite fraction after tensile deformation for all annealing conditions. (b) Volume fraction of austenite transformed to martensite, estimated from the ratio between the austenite fraction transformed to martensite for the fractured condition and the initial austenite fraction for the as-annealed condition. The volume fraction of austenite transformed to martensite increases with increasing annealing time. (c–d) EBSD analysis of the annealed, 5% deformed, and 10% deformed IA620-10 and IA620-24 specimens. The EBSD phase maps of (c_1)–(c_3) IA620-10 and (d_1)–(d_3) IA620-24 show a continuous decrease in the austenite volume fraction with increasing strain owing to the TRIP effect.

brittle zones (Fig. 13(a_3)–(f_3)). With increasing annealing time, the fraction of the ductile zones increases from 20% for the cold-rolled sample to 65% for specimen IA620-24, with a simultaneous decrease in the fraction of the brittle zones. The ductile zones are characterized by dimples, whereas the brittle zones show characteristics of cleavage and intergranular fracture. The change in fracture mechanism from brittle-dominant to ductile-dominant could be associated with a higher degree of recovery of tempered martensite and the formation of recrystallized ferrite/austenite grains.

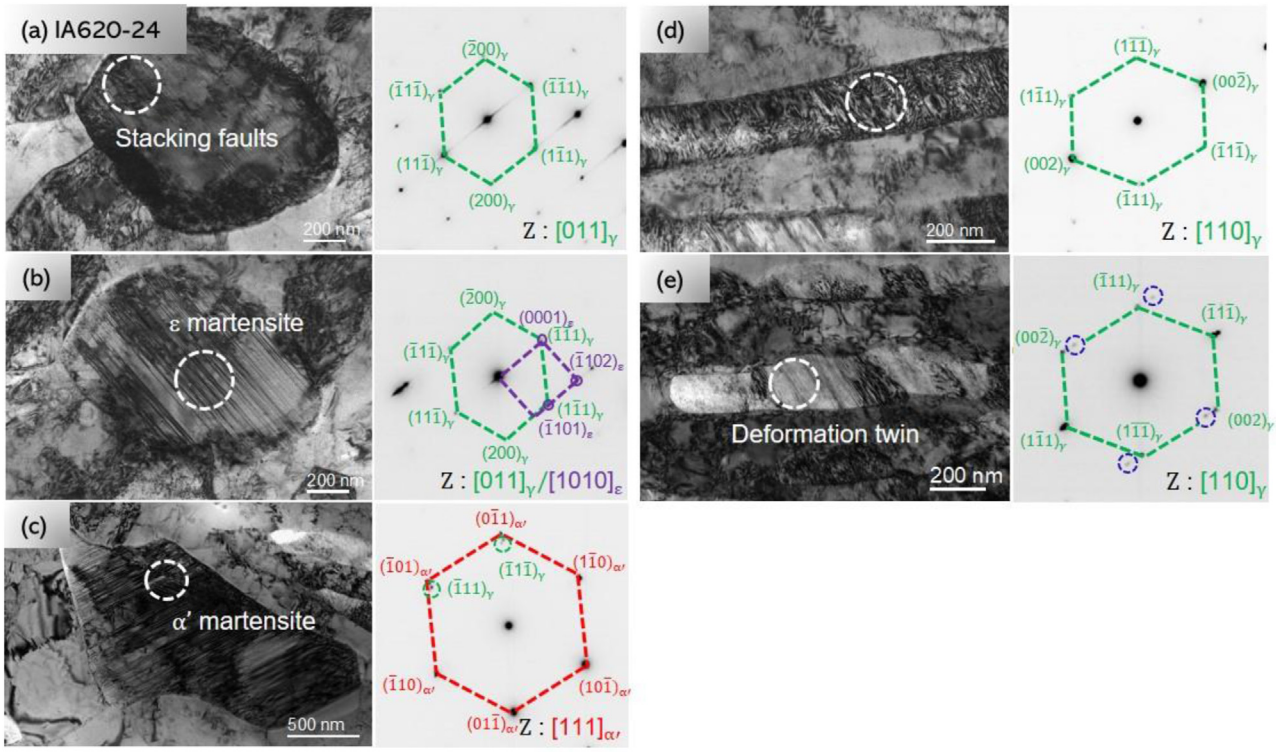

Fig. 10 – TEM analysis conducted for the 5% deformed IA620-24 specimen for (a–c) the equiaxed and (d–e) lath austenite grains. The equiaxed austenite grain in (a), (b), and (c) show stacking faults, ε-martensite, and α′ martensite, respectively. The lath austenite grain in (d) and (e) show high defect density without evidence of phase transformation and deformation twins, respectively.

4. Discussion

4.1. *Annealing time-dependent microstructure evolution*

The microstructural evolution of the cold-rolled material with increasing annealing time is shown in Fig. 2. The cold-rolled and annealed microstructures show a mixture of lath zone consisting of tempered martensite and lath austenite and equiaxed zone consisting of equiaxed ferrite/austenite and retained tempered martensite. With increasing annealing time, the fraction of the lath zone decreases and that of the equiaxed zone increases, leading to an increase in the fraction of recrystallized ferrite/austenite and a decrease in the fraction of tempered martensite (Fig. 4). The mixed presence of the lath and equiaxed zones could originate from different degrees of local deformation in the cold-rolled microstructure. A high level of local deformation, i.e., higher stored energy, in the cold-rolled microstructure can result in high recrystallization kinetics, thus producing an equiaxed zone containing

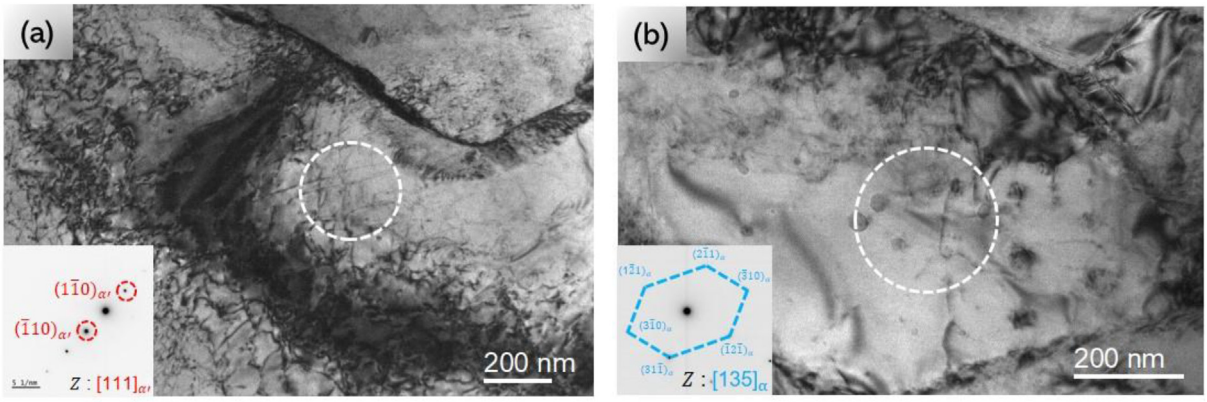

Fig. 11 – TEM analysis conducted for the 5% deformed IA620-24 specimen for the tempered martensite/ferrite grains. (a) Complex dislocation arrangement in the tempered martensite grain and (b) interactions between dislocations and B2 particles in the ferrite/martensite grain.

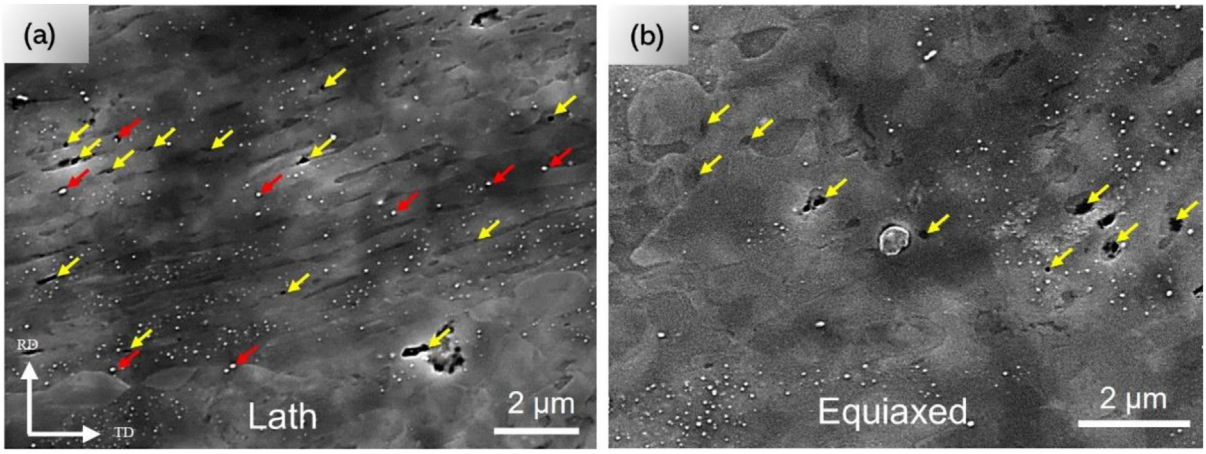

Fig. 12 – SEM analysis of the fractured microstructure. Voids or cracks are observed in the (a) lath zone and (b) equiaxed zone. For both regions, the areas decorated with a high density of white B2 particles correspond to tempered martensite grains. Voids or cracks indicated by the yellow arrows are associated with the austenite/martensite phase boundaries. Voids or cracks present near the B2 particles are indicated by red arrows.

recrystallized equiaxed ferrite/austenite grains. In contrast, a low level of local deformation can lead to sluggish recrystallization kinetics and the partially-recrystallized microstructure of the lath zone.

The deformed martensite in the cold-rolled microstructure undergoes recovery during annealing. The recovered martensite contains a lower dislocation density than the cold-rolled deformed martensite [24]. The high strain energy in the cold-rolled deformed martensite with a high dislocation density can be reduced by the rearrangement of dislocations during recovery, resulting in the formation of sub-grains [25]. The sub-grains are characterized by the presence of low-angle sub-boundaries formed by the rearrangement of dislocations [25]. Such sub-boundaries consist of a high density of dislocations accommodating a misorientation between neighboring sub-grains (Fig. 5(a) and (b)).

During the annealing of deformed medium Mn steels, the austenite phase has been reported to nucleate from Mn-decorated linear and planar defects [24,26]. Benzing et al. [24] reported the formation of two types of austenite morphology, i.e., equiaxed and rod/plate (lath)-type, during the annealing of deformed martensitic medium Mn steel. The equiaxed and lath austenite grains were nucleated at high-angle boundaries and lath/block boundaries, respectively [24,27–29]. The equiaxed ferrite grains were suggested to be formed by recovery-based recrystallization rather than true recrystallization involving nucleation and growth stages with the formation of high-angle grain boundaries [24]. Fig. 6(b) shows a low dislocation density equiaxed grain in region (2), which can be classified as ferrite, surrounded by the partially-recrystallized coarse grain with a relatively high dislocation density, which is expected to be tempered martensite. Thus, ferrite grains are

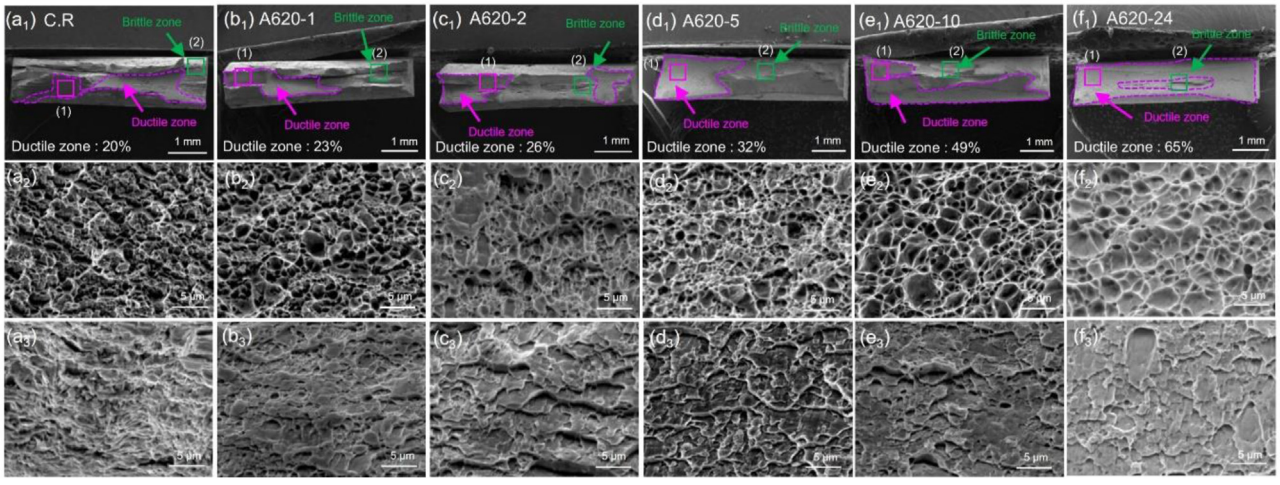

Fig. 13 – Fractography analysis of the fractured materials. (a_1)–(f_1) Overview fracture surfaces of the investigated materials. All the investigated materials exhibit a mixture of (a_2)–(f_2) ductile and (a_3)–(f_3) brittle zones. With increasing annealing time, the brittle zones decrease, and the ductile zones increase. The ductile zones are characterized by dimples, whereas the brittle zones show cleavages and characteristics of intergranular fracture.

expected to be formed by a decrease in dislocation density during the recovery of martensite (Fig. 5). The EBSD analysis (Fig. 4(g)) further supports a continuous transition from partially-recrystallized tempered martensite to recrystallized ferrite by the recovery process.

B2 precipitates are present in the deformed martensite of the cold-rolled material; these are expected to form during the hot-rolling process (Fig. 2(a)). The crystal structure of the B2 precipitates is almost same as that of the BCC ferrite/martensite phase, resulting in a low lattice misfit, decreased nucleation barrier, and the formation of highly dispersed, fully coherent nanoscale precipitates [22]. Thus, the present study also shows a higher density of B2 precipitates in the BCC ferrite/martensite phase than in the FCC austenite phase (Figs. 2 and 7). Coarse precipitates are mostly present near the ferrite/austenite grain/phase boundaries possibly owing to higher diffusivity at grain/phase boundaries (Fig. 2) [22,30]. Fig. S1 compares microstructures of specimens IA620-1 and IA620-24, showing formation and growth of some B2 particles at ferrite/austenite grain/phase boundaries during intercritical annealing.

4.2. *Microstructures-mechanical properties relationship*

With increasing annealing time, the investigated materials exhibit a decrease in YS (Fig. 8(a)) owing to a decrease in dislocation density and grain growth. With increasing annealing time, the dislocation density decreases owing to the recovery of martensite and the formation of recrystallized ferrite/austenite grains (Figs. 4 and 5), and the grain size of the recrystallized ferrite/austenite grains tends to increase, thereby leading to a decrease in grain size strengthening. Both factors lead to a decrease in YS with increasing annealing time. The role of precipitation hardening in the YS could not be precisely investigated owing to the difficulty in quantitative analysis of the nanoscale B2 precipitates. Therefore, the decreases in dislocation strengthening and grain size strengthening are expected to play significant roles in the decrease in YS with increasing annealing time.

The ductility and strain-hardening rate increase with increasing annealing time (Fig. 8(b)). Strain hardening of materials is governed by dislocation strengthening, which originated from the multiplication of dislocations and their interactions. When the initial dislocation density is low, multiplication of dislocations is much easier. Recrystallized ferrite and austenite grains with a low initial dislocation density could exhibit enhanced dislocation multiplication during deformation compared to tempered martensite with a high initial dislocation density. With increasing annealing time, the degree of recrystallization continuously increases in the microstructure, resulting in a decrease in a dislocation density after annealing, enhanced dislocation multiplication and strain hardening during deformation.

The TRIP effect also significantly affects the strain-hardening behavior of the investigated materials. The decrease in the mechanical stability of austenite with increasing annealing time is related to the decrease in the content of austenite-stabilizing elements such as Mn and Ni (Table 1) present in austenite and the grain growth of austenite (Fig. 4(f)). Thus, a large fraction of recrystallized grains and high TRIP kinetics can lead to the observed large strain-hardening rate and ductility for IA620-24. In the deformed IA620-24 specimen (Fig. 10), the equiaxed austenite grains exhibit various deformation mechanisms such as the formation of stacking faults, ε-martensite, α' martensite, whereas the lath austenite grains exhibit dislocations without phase transformation and deformation twinning. This indicates higher mechanical stability of lath austenite grains than that of equiaxed austenite grains [31,32]. The mixed presence of less stable equiaxed austenite and more stable lath austenite could lead to sustained TRIP effect during tensile deformation and superior strain hardening capacity of IA620-24.

The complex microstructures of the investigated materials showing a mixture of lath and equiaxed zones consist of a triplex matrix phase (ferrite, austenite, and tempered martensite) with B2 precipitates. Utilizing the hierarchical microstructural features and optimizing the annealing conditions can provide a superior balance between YS, UTS, TE, and damage tolerance, as evidenced by the absence of microcracks or the presence of very fine cracks near the B2 precipitates. The tensile properties of the specimen IA620-24 were compared with other B2-containing medium Mn steels processed by intercritical annealing [13,14,33–35], showing a similar strength-ductility balance with other steels (Fig. S2). The present study provides a novel microstructure design solution for medium Mn steels, and further optimization of the composition and processing will lead to the development of medium Mn steels with superior mechanical performance.

5. Conclusions

The present study reported the annealing time-dependent microstructure–mechanical properties relationship of cold-rolled and annealed Fe–6Mn-0.05C–3Ni-1.5Al (wt.%) steel, containing Ni and Al to form NiAl B2 precipitates. The conclusions drawn from the present study are as follows:

(a) The cold-rolled and annealed microstructure showed a mixture of lath and equiaxed zones. The lath zone consisted of tempered martensite and lath austenite, whereas the equiaxed zone consisted of tempered martensite and equiaxed ferrite/austenite. With increasing annealing time, the fraction of recrystallized ferrite/austenite increased and the fraction of tempered martensite decreased.
(b) B2 precipitates were present in the deformed martensite of the cold-rolled material; these precipitates are expected to be formed during the hot-rolling process. A higher density of B2 precipitates was observed in the BCC ferrite/martensite phase than in the FCC austenite phase. Coarse precipitates were mostly present near the ferrite/austenite grain boundaries.
(c) Deformed martensite in the cold-rolled microstructure experienced recovery during annealing, leading to the formation of sub-boundaries. These sub-boundaries contained a high density of dislocations accommodating a small misorientation between neighboring subgrains. The recovery process could lead to a contin-

uous transition from partially-recrystallized tempered martensite to recrystallized ferrite.

(d) The investigated materials showed a decrease in strength and an increase in ductility and strain-hardening rate with increasing annealing time. The decrease in the YS of the investigated materials with increasing annealing time attributed to decreases in the dislocation density and grain growth. A decrease in the fraction of tempered martensite, an increase in the fraction of recrystallized ferrite/austenite grains, and enhanced TRIP kinetics with increasing annealing time could lead to enhanced ductility and strain hardening of the materials. The mixed presence of less stable equi-axed austenite and more stable lath austenite could lead to sustained TRIP effect during tensile deformation and superior strain hardening capacity of IA620-24.

Declaration of competing interest

The authors declare that they have no known competing financial interests or personal relationships that could have appeared to influence the work reported in this paper.

Acknowledgement

This research was supported by the POSCO Science Fellowship of POSCO TJ Park Foundation, South Korea and by Korea Institute for Advancement of Technology (KIAT) grant funded by the Korea Government (MOTIE) (P0023676, HRD Program for Industrial Innovation).

Appendix A. Supplementary data

Supplementary data to this article can be found online at https://doi.org/10.1016/j.jmrt.2023.09.299.

REFERENCES

[1] Suh D-W, Kim S-J. Medium Mn transformation-induced plasticity steels: recent progress and challenges. Scripta Mater 2017;126:63–7.
[2] Lee S, De Cooman BC. On the selection of the optimal intercritical annealing temperature for medium Mn TRIP steel. Metall Mater Trans 2013;44(11):5018–24.
[3] Lee S, De Cooman BC. Tensile behavior of intercritically annealed 10 pct Mn multi-phase steel. Metall Mater Trans 2014;45(2):709–16.
[4] He B, Luo H, Huang M. Experimental investigation on a novel medium Mn steel combining transformation-induced plasticity and twinning-induced plasticity effects. Int J Plast 2016;78:173–86.
[5] Lee S, Lee K, De Cooman BC. Observation of the TWIP+ TRIP plasticity-enhancement mechanism in Al-added 6 wt pct medium Mn steel. Metall Mater Trans 2015;46:2356–63.
[6] Pan H, Ding H, Cai M. Microstructural evolution and precipitation behavior of the warm-rolled medium Mn steels containing Nb or Nb-Mo during intercritical annealing. Mater Sci Eng, A 2018;736:375–82.
[7] Lee D, Kim J-K, Lee S, Lee K, De Cooman BC. Microstructures and mechanical properties of Ti and Mo micro-alloyed medium Mn steel. Mater Sci Eng, A 2017;706:1–14.
[8] Yan S, Liang T, Chen J, Li T, Liu X. A novel Cu-Ni added medium Mn steel: precipitation of Cu-rich particles and austenite reversed transformation occurring simultaneously during ART annealing. Mater Sci Eng, A 2019;746:73–81.
[9] Li Y, Li W, Min N, Liu W, Jin X. Effects of hot/cold deformation on the microstructures and mechanical properties of ultra-low carbon medium manganese quenching-partitioning-tempering steels. Acta Mater 2017;139:96–108.
[10] Zhang B-G, Zhang X-M, Liu H-T. Microstructural evolution and mechanical properties of Ni-containing light-weight medium-Mn TRIP steel processed by intercritical annealing. Mater Sci Eng, A 2020;793:139289.
[11] Cai Z, Zhang K, Jing S, Ding H. Influence of nickel on microstructure and mechanical properties of medium-manganese steels. Mater Sci Technol 2019;35(1):68–76.
[12] Sun B, Palanisamy D, Ponge D, Gault B, Fazeli F, Scott C, et al. Revealing fracture mechanisms of medium manganese steels with and without delta-ferrite. Acta Mater 2019;164:683–96.
[13] Kumar S, Sarkar A, Prasad AD, Paliwal M, Mukherjee S, Mandal S. Superior strength-ductility combination in a Ni-modified medium manganese lightweight steel with the determining role of phase transformation and recrystallization behaviour. Mater Sci Eng, A 2022;835:142664.
[14] Sahoo BK, Srivastava VC, Chandan AK, Chowdhury SG. Enhancing the properties of Al–Ni added medium Mn steel by tailoring B2–NiAl precipitates through aging treatment. Mater Sci Eng, A 2022;837:142757.
[15] Kim J-K, Kim JH, Suh D-W. Partially-recrystallized ferrite grains and multiple plasticity enhancing mechanisms in a medium Mn steel. Mater Char 2019;155:109812.
[16] Li X, Song R, Zhou N, Li J. An ultrahigh strength and enhanced ductility cold-rolled medium-Mn steel treated by intercritical annealing. Scripta Mater 2018;154:30–3.
[17] Hu J, Du L-X, Xu W, Zhai J-H, Dong Y, Liu Y-J, et al. Ensuring combination of strength, ductility and toughness in medium-manganese steel through optimization of nano-scale metastable austenite. Mater Char 2018;136:20–8.
[18] Yang F, Luo H, Hu C, Pu E, Dong H. Effects of intercritical annealing process on microstructures and tensile properties of cold-rolled 7Mn steel. Mater Sci Eng, A 2017;685:115–22.
[19] Polkowski W, Jóźwik P, Bojar Z. EBSD and X-ray diffraction study on the recrystallization of cold rolled Ni3Al based intermetallic alloy. J Alloys Compd 2014;614:226–33.
[20] Luo J, Chu R, Yu W, Chen Y, Zhang C. Fine-grained processing and electron backscatter diffraction (EBSD) analysis of cold-rolled Inconel 617. J Alloys Compd 2019;799:302–13.
[21] Hadadzadeh A, Mokdad F, Wells M, Chen D. A new grain orientation spread approach to analyze the dynamic recrystallization behavior of a cast-homogenized Mg-Zn-Zr alloy using electron backscattered diffraction. Mater Sci Eng, A 2018;709:285–9.
[22] Jiang S, Wang H, Wu Y, Liu X, Chen H, Yao M, et al. Ultrastrong steel via minimal lattice misfit and high-density nanoprecipitation. Nature 2017;544(7651):460–4.
[23] Lo KH, Shek CH, Lai J. Recent developments in stainless steels. Mater Sci Eng R Rep 2009;65(4–6):39–104.
[24] Benzing JT, Da Silva AK, Morsdorf L, Bentley J, Ponge D, Dutta A, et al. Multi-scale characterization of austenite reversion and martensite recovery in a cold-rolled medium-Mn steel. Acta Mater 2019;166:512–30.

[25] Abbaschian R, Reed-Hill RE. Physical metallurgy principles-SI version. Cengage Learning; 2009.
[26] Kwiatkowski da Silva A, Ponge D, Peng Z, Inden G, Lu Y, Breen A, et al. Phase nucleation through confined spinodal fluctuations at crystal defects evidenced in Fe-Mn alloys. Nat Commun 2018;9(1):1–11.
[27] Trang T, Heo Y-U. The role of austenite stability on the change of fracture mode in a dual-phase medium Mn steel having a lamellar microstructure. Mater Char 2021;178:111264.
[28] Han J, da Silva AK, Ponge D, Raabe D, Lee S-M, Lee Y-K, et al. The effects of prior austenite grain boundaries and microstructural morphology on the impact toughness of intercritically annealed medium Mn steel. Acta Mater 2017;122:199–206.
[29] Zhou T, Wang C, Wang C, Cao W, Chen Z. Austenite stability and deformation-induced transformation mechanism in cold-rolled medium-Mn steel. Mater Sci Eng, A 2020;798:140147.
[30] Zhang B-G, Zhang X-M, Wang G-D, Liu H-T. Age-hardening medium Mn steel with high strength and large ductility. Mater Sci Eng, A 2019;756:35–40.
[31] Xiong X, Chen B, Huang M, Wang J, Wang L. The effect of morphology on the stability of retained austenite in a quenched and partitioned steel. Scripta Mater 2013;68(5):321–4.
[32] Sahoo BK, Srivastava VC, Chandan AK, Chhabra HS, Chowdhury SG. Evolution of microstructure and deformation behavior in Al–Ni added medium-Mn steel processed through intercritical/cold rolling and annealing. Mater Sci Eng, A 2021;824:141852.
[33] Zou Y, Xu Y, Wang G, Han Y, Teng H, Han D, et al. Improved strength-ductility-toughness balance of a precipitation-strengthened low-carbon medium-Mn steel by adopting intercritical annealing-tempering process. Mater Sci Eng, A 2021;802:140636.
[34] Song H, Yoo J, Kim S-H, Sohn SS, Koo M, Kim NJ, et al. Novel ultra-high-strength Cu-containing medium-Mn duplex lightweight steels. Acta Mater 2017;135:215–25.
[35] Li Y, Li W, Li J, Xin S, Min N, Liu W, et al. Characterization and 3D finite element modelling of TRIP effect in a medium manganese steel with nano-precipitates. Mater Char 2021;172:110845.